COMPARISON OF THE CRACK PATTERN IN ACCELERATED CORROSION TESTS AND IN FINITE ELEMENTS SIMULATIONS

B. Sanz[1], J. Planas[1], J.M. Sancho[2]

[1]Departamento de Ciencia de Materiales, E.T.S. de Ingenieros de Caminos, Canales y Puertos, Universidad Politécnica de Madrid, C/ Profesor Aranguren s/n, 28040 Madrid, España.
E-mail: bsanz@mater.upm.es
E-mail: jaime.planas@upm.es

[2]Departamento de Estructuras de Edificación, E.T.S. de Arquitectura, Universidad Politécnica de Madrid, Avda. Juan de Herrera 4, 28040 Madrid, España.
E-mail: jose.sancho@upm.es

ABSTRACT

In this work, the crack pattern obtained in accelerated corrosion tests is compared to the one obtained in numerical simulations for reinforced steel concrete samples. In the simulations, an expansive joint element is used to simulate the oxide layer behaviour together with finite elements with embedded adaptable cohesive crack to simulate the concrete fracture. In parallel, some samples are artificially corroded imposing constant current and after corrosion they are impregnated with resin containing fluorescein to improve the detection of the cracks. In the paper, the main features of the model and the experimental procedure are described and the crack pattern is analysed. A main crack across the concrete cover is easily seen in both cases, but also secondary cracks are observed after treating the concrete surface, in accordance with the model predictions, which gives further support to the ability of the numerical approach to simulate the real cracking processes.

KEY WORDS: Accelerated corrosion tests, Cohesive crack, Finite Elements simulations

1 INTRODUCTION

Corrosion of rebars is an important pathology in reinforced steel concrete structures. It consists of the generation of an oxide layer at the steel surface that induces internal pressure on the surrounding concrete, due to the greater specific volume of the oxide with respect to the steel, and thus cracks the concrete cover [1, 2, 3].

Focussing on the prediction of the mechanical effects of the oxide expansion over the concrete, a numerical model to simulate the oxide layer behaviour was programmed, assuming that the corrosion depth is given at any specified time [4]. It was called *expansive joint element* and it has already been presented in previous conferences. That model consists in an interface element with zero initial thickness that incorporates both the expansive and the mechanical behaviour of the oxide, which is characterised by its debonding ability, with nearly free sliding (very small shear stiffness) and nearly free separation (strongly reduced normal tension stiffness). Concrete cracking is simulated by finite elements with embedded adaptable cohesive cracks [5] that follow the basic cohesive crack model proposed by Hillerborg et al [6].

In parallel, accelerated corrosion tests have been carried out in order to verify the ability of the model to simulate real processes. The samples are concrete prisms with a steel tube inside simulating a rebar, that are artificially corroded by the imposition of constant current. After corrosion, the samples are cut into slices to study the cracking along the bar and they are impregnated under vacuum with resin containing fluorescein to improve the detection of the cracks.

The crack pattern obtained in the tests is compared to the one obtained in numerical simulations of the same process. In both cases, a main crack is observed from the steel to the concrete surface, but also some secondary cracks and some microcracks can be seen when looking under the microscope or after impregnating the concrete surface with resin and fluorescein, in accordance to the model predictions.

In the paper, the main features of the model and the experimental procedure are described and the crack pattern is analysed.

2 NUMERICAL SIMULATIONS

2.1 Finite element model

In the simulations, finite elements with embedded adaptable cohesive crack [5] are used to model the concrete cracking. Those elements follow the basic cohesive crack model [6] and they are programmed in C++ within the finite element framework COFE (*Continuum Oriented Finite Elements*).

To model the oxide layer behaviour, an interface finite element called *expansive joint element* was programmed

by the authors [4] within the finite element framework COFE. It consists in a four-node element with zero initial thickness and it is defined by the initial length and the normal direction. The model works assuming elastic behaviour, small strain and direct integration at the nodes. The main parameters of the model are the corrosion depth x (the amount of steel that is transformed into oxide) and a factor β that indicates the volumetric expansion of the oxide respect to the initial steel section and which depends on the ratio of the specific volumes of oxide and steel. A sketch of the model is shown in figure 1. It must be remarked that only the part corresponding to the volumetric expansion is considered as expansive joint element and the steel section is kept constant during the calculations, so mechanical equivalence between the element and the real oxide needs to be established. The main equations of the model are detailed in the appendix at the end of the paper.

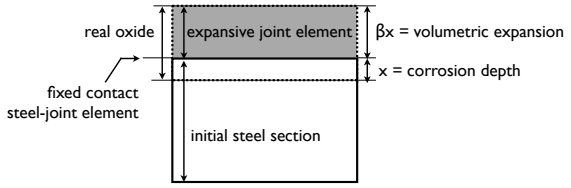

Figure 1: Sketch of the expansive joint element

2.2 *Parameters of the simulations*

The samples in the simulations are concrete prisms of 90 mm height and 100 mm width with a 20 mm diameter smooth steel bar cast-in, centred with respect to the width, and with a concrete cover equal to the diameter of the bar. The concrete is modelled with elements with embedded adaptable cohesive crack, the steel with linear elastic elements and the oxide with expansive joint elements. The mesh is generated using the pre-post FE mesh processor Gmsh [7]. The elements are constant strain triangles.

The mechanical properties of steel and concrete were experimentally determined by mechanical tests (compression, brazilian and three point bending tests) [8, 9, 10, 11], so the parameters of the materials in the simulations are the same as the real ones. They are shown in table 1.

Two *linear* approximations for the softening curve have been used. The first one has a fracture energy $G_F = 0.1$ N/mm (100 N/m), which corresponds to the actual total fracture energy of the material, and, except for the tail, lies well above the actual softening function, as shown in Fig. 2. The second one has a fracture energy $G'_F = 0.5G_F = 0.05$ N/mm (50 N/m) and corresponds to the linear approximation of the initial portion of the softening curve, as shown in Fig. 2. These approximations provide lower and upper bounds for the brittleness of the behaviour.

However, there are no experimental results available for the properties of the oxide, so the values have to be assumed at a this stage of the research and need to be verified in future by tests. A value equal to one is assumed for β as found in the literature [2] and the other values have been chosen to have a reasonable stiffness for the oxide layer in compression while keeping the computations stable. A previous study revealed some essential features of the model: first, nearly free sliding, that is obtained by reduced shear stiffness, and second, nearly free separation, that is obtained by strongly reduced stiffness in tension. The adopted values are shown in table 2. The total radial expansion is 25 μm and it is imposed in 50 steps.

Table 1: Mechanical properties of steel and concrete, where E is the elasticity modulus, ν is the Poisson coefficient, α' is the adaption factor of the crack, f_t is the tensile strength and G_F is the fracture energy.

	Steel	Concrete
E (GPa)	200	30
ν	0.3	0.2
α'	–	0.2
f_t (MPa)	–	3.0
G_F (N/mm)	–	0.1

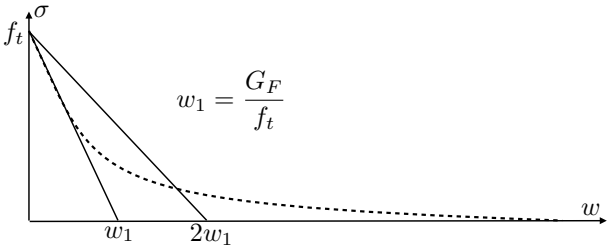

Figure 2: Sketch of the curvilinear softening curve, and the two linear approximation used in the paper

Table 2: Properties of the oxide, where β is the volumetric expansion factor, x_0 is the cut-off corrosion depth, k^0_{nc} is the initial compression stiffness, k^0_t is the initial shear stiffness and η_t is the directionality factor.

β	1.0
x_0 (mm)	$1.0e^{-3}$
k^0_{nc} (N/mm^3)	$7.0e^{6}$
k^0_t (N/mm^3)	$7.0e^{-14}$
η_t	$1.0e^{-11}$

2.3 *Crack pattern obtained in the simulations*

The crack patterns obtained in the simulations are shown in Figs. 3 and 4 for corrosion depths x of 4 and 25 μm, respectively. The crack width (in mm) and the maximum principal stress (in MPa) are represented; the top picture in each figure corresponds to linear softening with $G_F = 0.1$ N/mm and x100 magnification of displacements and the bottom one to the linear softening with $G'_F = 0.05$ μm, and undeformed mesh.

Figure 3 shows that in both cases a main crack has formed across the concrete cover, while a ring of radial cracks of similar extent forms around the bar; the only difference is that for the tougher softening the crack width nowhere exceeds 6.7 μm, while for the more brittle softening reaches a width of 10.5 μm at the concrete surface; this is closer to the expected behaviour, since the maximum opening is well within the initial linear portion of the softening curve ($w_1 = 33.6$ μm in Fig. 2).

Figure 4 shows that the main crack width for $x = 25$ μm is very similar for the two softening lines (122 vs. 124 μm); however, the secondary crack pattern is much more localised in the more brittle concrete.

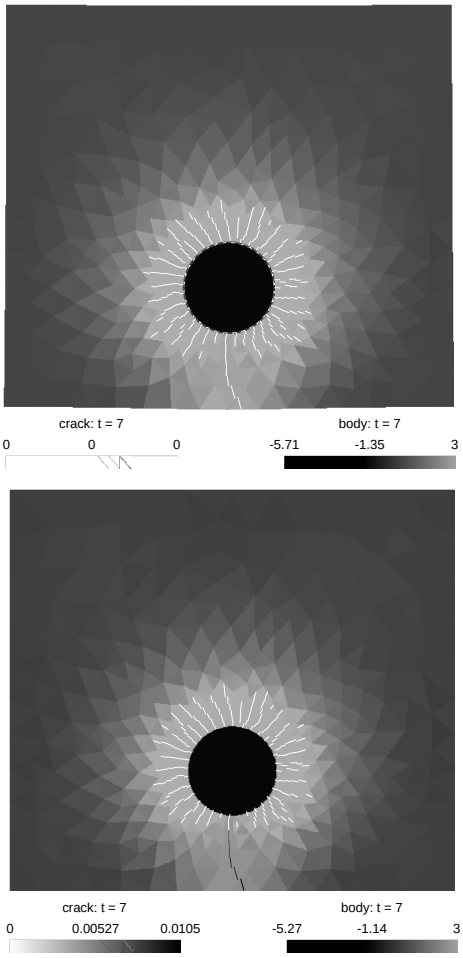

Figure 3: Crack pattern for a corrosion depth of 4μm for linear softening with $G_F = 0.1$ N/mm (top) and $G_F = 0.05$ N/mm (bottom).

3 EXPERIMENTAL PROCEDURE

3.1 Accelerated corrosion tests

The samples are concrete prisms with the same cross-sectional dimensions of the simulated prisms, with the bar substituted by a steel tube of the same outer diameter (20 mm).

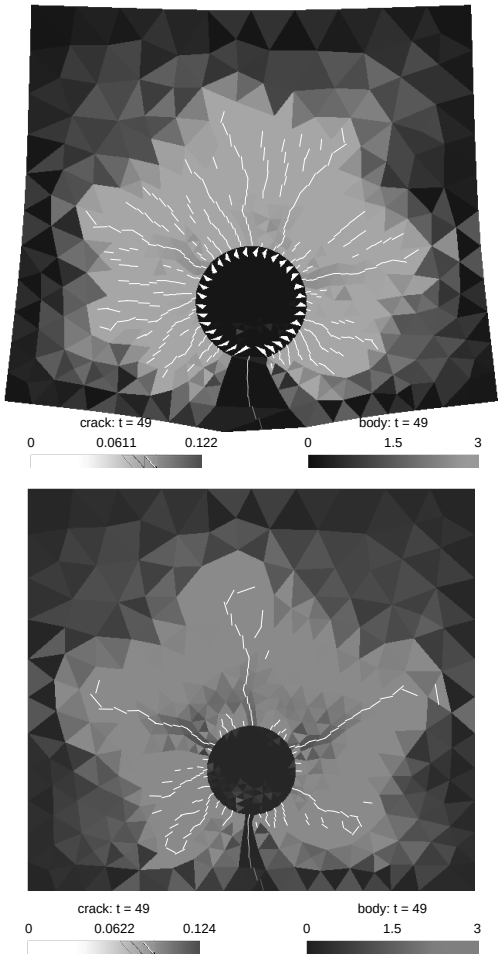

Figure 4: Crack pattern for a corrosion depth of 25μm for linear softening with $G_F = 0.1$ N/mm (top) and $G_F = 0.05$ N/mm (bottom).

The samples were artificially corroded by the imposition of a constant current density of 400 μA/cm^2. This current is much higher than the maximum values observed in actual structures, which may affect to the type of oxide that is generated, but these tests are only intended to analyse crack patterning and the ability of the numerical approach to reproduce it; slower tests will be conducted in the future. The imposition of the current was maintained until a noticeable crack appeared at the concrete surface. The counter electrode was a tube of stainless steel and the conductor medium was water without any additives. The sample is placed with the tube in vertical position. Figure 5 shows a view of the test assembly.

After corrosion, the samples were cut into four slices with a radial saw and a grinding machine was used to improve the smoothness of the surfaces of the cuts. A picture of one of the central slices is shown in figure 6. A main crack is easily seen across the concrete cover, in good agreement with the numerical predictions; a much thinner crack opposite to the main crack is hardly visible, but detecting further secondary cracks requires the help of magnifying devices.

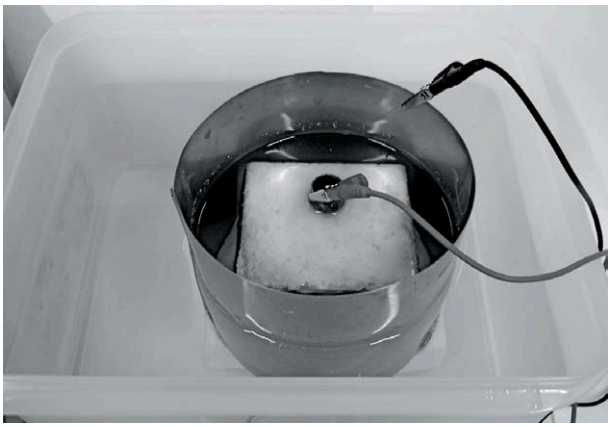

Figure 5: View of the assembly of an accelerated corrosion tests

When looking under the microscope, thin secondary cracks and radial micro-cracks are detected, in accordance with the results of the simulations, as shown in figures 7 and 8. Bright vertical lines on the steel surface can be observed that have been produced during the grinding process.

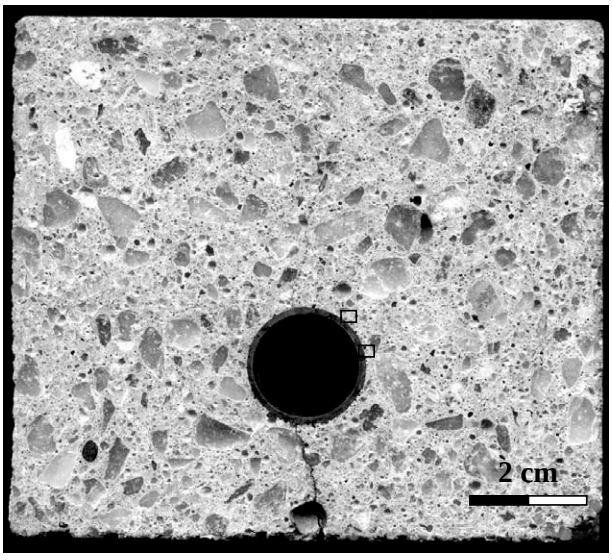

Figure 6: General view of the crack pattern observed in a corroded sample

3.2 Resin impreganation

In order to improve the detection of the cracks, the slices were impregnated with resin and fluorescein under vacuum. A low viscosity resin was selected to facilitate its penetration. The concentration of fluorescein was adjusted by selecting among a set of five concentrations the smaller concentration that delivered good visibility of the mix under ultra violet (UV) light; a concentration of $1,5$ mg of fluorescein per millilitre of resin was finally used.

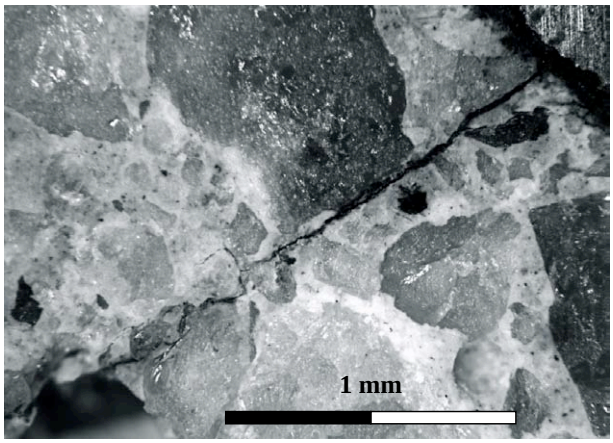

Figure 7: Secondary cracks observed in a corroded sample when looking under the microscope

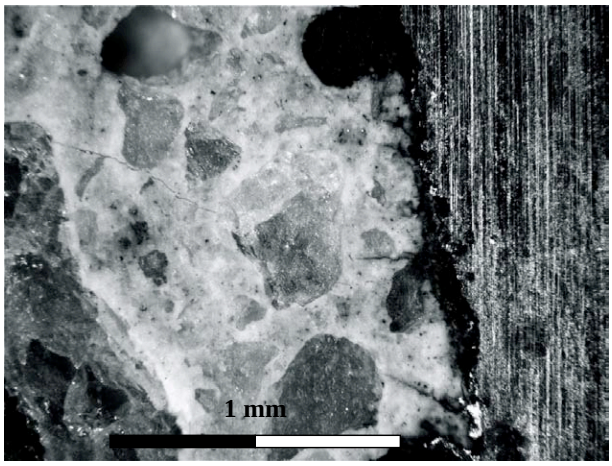

Figure 8: Radial micro-cracks observed in a corroded sample when looking under the microscope

The slices were impregnated under vacuum to improve the resin penetration through the cracks and pores of concrete. For that, a vacuum pump and a pressure cooker were utilised. A vacuum of 600 mmHg was reached. Firstly, vacuum was applied to the slice of concrete to empty of air the pores. Then, the resin was injected while keeping the vacuum. And finally the valve that controls vacuum was opened allowing the air to get inside. After curing the resin during two days at room temperature, the surfaces of the resin were ground again to eliminate the excess of resin and to expose undisturbed material.

In figure 10 a picture of the same slice that was studied in figures 6-8 is shown after impregnation and under UV lighting. The secondary cracks and some microcracks that were only observable under microscope before applying the surface treatment are now easily seen, and the overall pattern strikingly resembles the pattern in figure 4.

A further interesting observation is that the main crack, which can be seen by the naked eye without impregna-

tion, does not seem to have taken much resin during impregnation. The reason seems to be that the crack is full of compact black iron oxide. This seems to be true also for the root (next to the steel) of some secondary cracks.

Figure 9: Vacuum impregnation assembly. Pump, control of the pump and pressure cooker

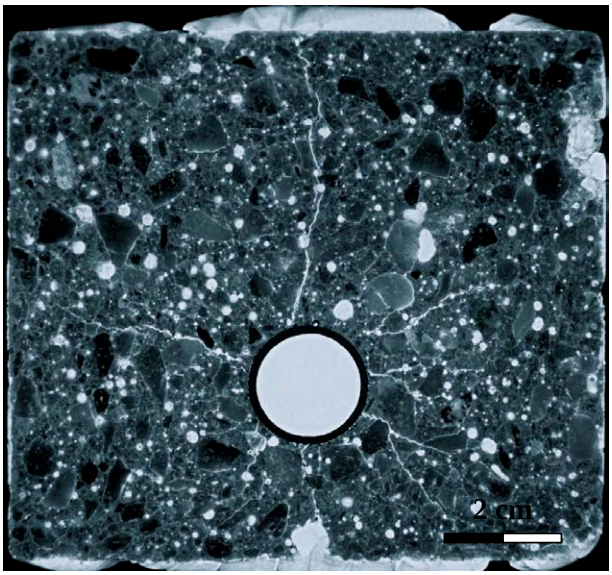

Figure 10: General view of the crack pattern obtained in a corroded sample after impregnating the surface with resin and fluorescein and lighting it with UV light

4 CONCLUSIONS

An interface finite element called *expansive joint element* was programmed to simulate the expansion of the oxide layer that is generated when the rebars in reinforced concrete structures are corroded and to study the mechanical effects of it over the surrounding concrete. The simulations with that model predict a wide main crack across the concrete cover but also six or seven long secondary cracks and other smaller cracks, all of them much less opened than the main crack.

Very similar results are obtained when acceleratedly corroding real samples. Although only the main crack is clearly visible by the naked eye, secondary cracks and microcracks can be seen under the microscope, although in this way the wide-field view is lost, unless a wide micrograph covering is built.

The wide-field crack detection can be achieved by vaccuum-impregnating the samples with low viscosity resin containing fluorescein and observing them under UV light. The overall pattern of the fluorescent cracks closely resembles the patterns obtained numerically. The main crack and the root of some of the secondary cracks seems to be filled up with compact oxide.

ACKNOWLEDGEMENTS

The authors gratefully acknowledge the *Ministerio de Ciencia e Innovación, Spain,* for providing financial support for this work under grant BIA2005-09250-C03-01, and for providing, within the Spanish National Research Program CONSOLIDER-INGENIO 2010, funds for the research framework SEDUREC, within which the authors carried out their work. The authors also thank Mr. José Miguel Martínez for his help and advice during the setup of the experiments.

REFERENCES

[1] C. Andrade, M.C. Alonso, and F.J. Molina. Cover cracking as a function of bar corrosion: Part i - experimental test. *Materials and Structures*, 26:453–464, 1993.

[2] F.J. Molina, M.C. Alonso, and C. Andrade. Cover cracking as a function of bar corrosion: Part ii - numerical model. *Materials and Structures*, 26:532–548, 1993.

[3] M.C. Alonso, C. Andrade, J. Rodriguez, and J.M. Diez. Factors controlling cracking of concrete affected by reinforcement corrosion. *Materials and Structures*, 31:435–441, 1997.

[4] B. Sanz, J. Planas, A. M. Fathy, and J. M. Sancho. Modelización con elementos finitos de la fisuración en el hormigón causada por la corrosión de las armaduras. *Anales de Mecánica de la Fractura*, 25:623–628, 2008.

[5] J. M. Sancho, J. Planas, D. A. Cendon, E. Reyes, and J. C. Galvez. An embedded cohesive crack model for finite element analysis of concrete fracture. *Engineering Fracture Mechanics*, 74:75–86, 2007.

[6] A. Hillerborg, M. Modéer, and P.E. Petersson. Analysis of crack formation and crack growth in concrete by means of fracture mechanics and fracture elements. *Cement and concrete research*, 6:773–782, 1976.

[7] C. Geuzaine and J.-F. Remacle. Gmsh: a three-dimensional finite element mesh generator with built-in pre- and post-processing facilities. *International Journal for Numerical Methods in Engineering*, 79(11):1309–1331, 2009.

[8] G. V. Guinea, J. Planas, and M. Elices. A general bilinear fitting for the softening curve of concrete. *Materials and Structures*, 27:99–105, 1994.

[9] M. Elices, G. V. Guinea, and J. Planas. On the measurement of concrete fracture energy using three point bend tests. *Materials and Structures*, 30:375–376, 1997.

[10] J. Planas, G. V. Guinea, and M. Elices. Size effect and inverse analysis in concrete fracture. *International Journal Fracture*, 95:367–378, 1999.

[11] J. Planas, G. V. Guinea, J. C. Galvez, B. Sanz, and A. M. Fathy. Experimental determination of the stress-crack opening curve for concrete in tension. report 39. chapter 3. indirect tests for stress-crack opening curve. Technical report, RILEM TC 187-SOC Final Report, 2007.

APPENDIX: EQUATIONS OF THE EXPANSIVE JOINT ELEMENT

The *expansive joint element* is defined by two parameters as explained in the main text: the corrosion depth x and the volumetric expansion factor β. The latter depends on the relation between the specific volumes of oxide and metal (per mole of metal):

$$\beta = \frac{v_{ox}}{v_{met}} - 1 \tag{1}$$

When external actions are applied simultaneously to the expansion of the oxide, the traction vector $\mathbf{t}$ can be assumed (in the simplest model) to be linearly related to the apparent mechanical displacement $\mathbf{w}^a$ and thus written as

$$\mathbf{t} = \mathbf{K_n}\mathbf{w}^a \qquad \text{with} \qquad \mathbf{w}^a = \mathbf{w} - \beta x \mathbf{n}, \tag{2}$$

where $\mathbf{K_n}$ is the stiffness tensor, $\mathbf{w}$ is the total displacement, $\mathbf{n}$ is the unit normal vector to the metal surface, and $\mathbf{w}^a$ is calculated as the difference between the total displacement and the free expansion displacement of the oxide. The stiffness tensor $\mathbf{K_n}$ is a second order and objective tensor that explicitly depends on the unit vector $\mathbf{n}$. It can be separated into the normal and tangent projections to the surface as

$$\mathbf{K_n} = k_n \mathbf{n} \otimes \mathbf{n} + k_t(\mathbf{1} - \mathbf{n} \otimes \mathbf{n}) \tag{3}$$

where $\mathbf{1}$ is the second order identity tensor, $\otimes$ expresses tensorial product of two vectors and k_n and k_t are the normal and tangent stiffness constants. Substituting equation (3) in equation (2), the stresses vector is finally given by

$$\mathbf{t} = k_n(\mathbf{w} \cdot \mathbf{n} - \beta x)\mathbf{n} + k_t[\mathbf{w} - (\mathbf{w} \cdot \mathbf{n})\mathbf{n}] \tag{4}$$

Considering a pure shear stress τ that is applied to the oxide surface, the real displacement u at the application point is given by the sum of the shear displacement of the metal layer plus that of the oxide layer:

$$u = h - x\frac{\tau}{G_{met}} + (1+\beta)x\frac{\tau}{G_{ox}} \tag{5}$$

where h is the height of the layer of steel and G_{met} and G_{ox} are the shear stiffness moduli of metal and oxide. The same displacement is calculated using the expansive joint element (which does not subtract thickness to the metal layer) as

$$u = h\frac{\tau}{G_{met}} + \frac{\tau}{k_t} \tag{6}$$

Mechanical equivalence between the expansive joint element and the real metal-oxide system is established by identifying the displacements given by equations (5) and (6), so that the expansive joint shear stiffness is given by

$$k_t = \frac{G^*_{ox}}{\beta x}, \text{ with } G^*_{ox} = \frac{\beta G_{ox}}{1+\beta}\left[1 - \frac{G_{ox}}{(1+\beta)G_{met}}\right]^{-1} \tag{7}$$

where G^*_{ox} is the equivalent transversal stiffness modulus of the expansive joint element. Imposing mechanical equivalence when a normal stress is applied, similar results are obtained for the normal stiffness:

$$k_n = \frac{K^*_{ox}}{\beta x}, \text{ with } K^*_{ox} = \frac{\beta K_{ox}}{1+\beta}\left[1 - \frac{K_{ox}}{(1+\beta)K_{met}}\right]^{-1} \tag{8}$$

where K^*_{ox}, K_{ox} and K_{met} are the normal stiffness moduli of the expansive joint element, the oxide and the metal. It turns out, from the foregoing equation, that stiffness moduli of the element are inversely proportional to the corrosion depth x. To avoid numerical instability, a cut-off stiffness is established for a certain small value x_0 of corrosion depth and thus we write where k^0_t and k^0_n are the shear and normal stiffness corresponding to x_0.

$$k_t = \begin{cases} k^0_t \\ k^0_t \dfrac{x_0}{x} \end{cases}, k_n = \begin{cases} k^0_n & \text{if } x \le x_0 \\ k^0_n \dfrac{x_0}{x} & \text{if } x > x_0 \end{cases} \tag{9}$$

In the model, there is the possibility to distinguish two cases of normal stiffness for compression and tension. It is introduced by a directionality factor η so that

$$k^0_n = \eta k^0_{nc} \tag{10}$$

where k_{nc} is the value of the stiffness for compression and η is given by

$$\eta = \begin{cases} 1 & \text{if } \mathbf{w} \cdot \mathbf{n} - \beta x \le 0 \text{ (compression)} \\ \eta_t & \text{if } \mathbf{w} \cdot \mathbf{n} - \beta x > 0 \text{ (tension).} \end{cases} \tag{11}$$

where η_t is a constant much less than one.